

Pumping metallic nanoparticles with spatial precision within magnetic mesoporous platforms: 3D Characterization and Catalytic Application

Nuria Miguel-Sancho,[‡] Gema Martinez,^{, †, ‡} Victor Sebastian,[†] Ana Malumbres,^{†, ‡} Ileana Florea,[§] Raul Arenal,^{‡, ⊥} M Carmen Ortega-Liebana,^{†, ‡} Jose L Hueso,^{†, ‡} and Jesus Santamaria,^{*, †, ‡}*

[†] Networking Research Center on Bioengineering, Biomaterials and Nanomedicine, CIBER-BBN, 28029 Madrid, Spain.

[‡] Department of Chemical and Environmental Engineering and Institute of Nanoscience of Aragon (INA), University of Zaragoza, 50018-Zaragoza, Spain.

[§] Laboratoire de Physique des Interfaces et des Couches Minces – LPICM École Polytechnique/CNRS, Route de Saclay, 91128 Palaiseau Cedex, (France).

^{||} Advanced Microscopy Laboratory (LMA), Nanoscience Institute of Aragon (INA), 50018-Zaragoza, Spain.

[⊥] Araid Foundation.

KEYWORDS

Recyclable, magnetically recoverable self-assembled structures, mesoporous silica, water-dispersible nanoparticles, magnetic properties, peptide-like bonding and hydrogenation.

ABSTRACT

The present work shows an efficient strategy to assemble two types of functional nanoparticles onto mesoporous MCM-41 silica nanospheres with high degree of spatial precision. In a first stage, magnetite nanoparticles are synthesized with a size larger than the support pores and grafted covalently through a peptide-like bonding onto its external surface. This endowed the silica nanoparticles with a strong superparamagnetic response, while preserving the highly ordered interior space for the encapsulation of other functional guest species. Secondly, we report the finely controlled pumping of preformed Pt nanoparticles (1.5 nm) within the channels of the magnetic MCM-41 nanospheres to confer an additional catalytic functionality to the multi-assembled nanoplatform. The penetration depth of the metallic nanoparticles can be explained as a result of the interplay between particle-wall electrostatic attraction and the repulsive forces between neighbouring Pt nanoparticles. A detailed transmission electron microscopy (TEM) and 3-D High-Resolution HAADF electron Tomography study was carried out to characterize the material and to explain the assembly mechanism. Finally, the performance of these multifunctional nanohybrids as magnetically recoverable catalysts has been evaluated in the selective hydrogenation of p-nitrophenol, a well-known pollutant and intermediate in multiple industrial processes.

1. INTRODUCTION

The assembly of two or more different nanostructured material with highly desirable properties, such as, ordered silica mesoporous framework (loading space and high surface area to host functional moieties), magnetic nanoparticles (superparamagnetic behaviour, magnetic separation/steering) and metal nanoparticles (catalytic, bactericidal or plasmonic properties) has been subjected to intense scientific and technological studies because of the wide range of potential applications of the resulting nanocomposites in the catalysis, environmental remediation and biomedical fields.¹⁻⁷ However, the design and fabrication of these multifunctional nano-sized structures is always a challenging task due to the inherent difficulties involved in a controlled assembly of the individual nano-constituents. A commonly exploited synthesis strategy involves the generation of silica-based magnetic mesoporous supports prior to the addition of a third functional component. In this regard, three representative configurations of magnetic silica mesoporous supports have been mostly postulated and evaluated: i) encapsulation of magnetic cores within a mesoporous silica shell,⁸ ii) filling the channels of ordered mesoporous materials with magnetic nanoparticles (NPs),⁹ iii) direct assembly of magnetic NPs onto the outer surface of silica nanostructures.¹⁰ The first strategy is carried out after growing a mesoporous silica shell around a magnetic core to form core magnetic-nanoparticles/mesoporous-silica core/shell nanostructures.^{8, 11-12} The major limitations to this process stem from the difficulties to prevent the formation of irregular core/shell structures¹³ and the low magnetization saturation values reached because of the low mass fractions of magnetic cores typically encapsulated.¹⁴⁻¹⁶ Whilst the second general synthesis approach allows a finer control of the magnetic particles in terms of size and shape due to pore diameter restrictions, often lacks of a precise and homogeneous distribution that

result in pore blocking, reduction of specific surface area or distortion of the ordered structures.⁹

17-18

As an alternative to overcome these drawbacks, the third strategy aims to assemble magnetic nanoparticles onto the surface of mesoporous silica nanostructures as a way to preserve both the magnetic response (that may even be enhanced due to synergistic magnetism¹⁹⁻²¹) and a regular porous structure capable to host functional guest species as demonstrated by Hyeon and co-worker.¹⁰ They reported an elegant method for the fabrication of magnetic mesoporous silica sphere assemblies with an unobstructed pore system. The key step was the direct nucleophilic substitution reaction between the amino groups on the surface of the mesoporous silica particles and the 2-bromo-2-methyl-propionic acid molecules coating the magnetic nanoparticles.²²⁻²³ In the resulting nanocomposites, the magnetic nanoparticles were uniformly distributed and bound tightly to the mesoporous silica nanospheres. Hence, the pore system remained fully accessible for hosting additional guest molecules despite of the previous anchoring of the magnetic particles. Encapsulation of a molecular chemotherapeutic agent as doxorubicin for drug delivery purposes was successfully demonstrated by the authors.¹⁰ However, this protocol involves the use of toxic solvents, such as dimethylformamide or chloroform, requires a large number of synthetic steps and further treatment with polyethylene glycol to make the obtained magnetic composite nanoparticles dispersible in aqueous media.

In spite of these drawbacks, this latter synthesis strategy appears to be one of the most promising pathways to develop robust multifunctional tri-component nanohybrids and was used as the starting point for ours. In this work we aim to incorporate a catalyst, specifically pre-formed platinum Pt nanoparticles, into the magnetic mesoporous MCM-41silica host, while preserving their dispersion and catalytic properties, and to do so with a high degree of spatial precision. We

present a novel size-exclusion strategy that allows a highly precise segregation of magnetic (outside) and metal nanoparticles (inside) on ordered porous silica nanoparticles. The assembly of functionalized superparamagnetic iron oxide nanoparticles exclusively on the external surface of MCM-41 nanoparticles has been carried out under mild condition in aqueous media with the aid of an easy, robust and straightforward peptide-like bonding, thereby overcoming the main problems derived from the Hyeon's method. Then, small (1.5 nm) monodisperse Pt nanoparticles have been "electrostatically pumped" into the mesoporous silica channels. The strategic coating of the Pt nanoparticles provided a high (-30 mV) negative surface charge that was instrumental in attaining a strong adhesion to the amino-functionalized silica support. In addition, a sufficiently high repulsion among nanoparticles provided the "pumping" effect and propelled them within the channels. The resulting nanohybrids have a high catalyst loading as demonstrated by the 3D Tomography analyses, and a strong magnetic response, while preserving the access to the catalyst active sites. Finally, we have demonstrated their potential as magnetically recoverable catalysts in a model selective hydrogenation reaction.

2. EXPERIMENTAL SECTION

2.1. Chemicals. Experiments were carried out by using commercially available analytical-grade reagents without further purification. Absolute ethanol, 3-aminopropyltriethoxysilane (APTES, 99%), ammonium hydroxide solution (30%), ethyl acetate, iron(III) acetylacetonate ($\text{Fe}(\text{acac})_3$), meso-2,3-dimercaptosuccinic acid (DMSA), sodium hydroxide, toluene, triethylene glycol (TREG), tetrakis(hydroxymethyl)phosphonium chloride solution (THPC, 80% wt.), chloroplatinic acid 8 wt% solution (H_2PtCl_6), p-Nitrophenol (4-NP) and sodium borohydride (NaBH_4 , 98%) were

purchased from Sigma-Aldrich. The experiments have been performed at the platform of Production of Biomaterials and Nanoparticles of the NANBIOSIS ICTS, Spain

2.2. Synthesis of amino-functionalized MCM-41 nanospheres. MCM-41 was synthesized following a previously reported method.²⁴⁻²⁵ The surface of the MCM-41 was functionalized with amino groups by treatment with 3-Aminopropyl triethoxysilane (APTES). MCM-41 (1.0 g) was dispersed in toluene (20 mL). The suspension was heated until reflux and then APTES (2.0 mL) was added. The solution refluxed for 7 h. After centrifugation and washing twice with ethanol, amine-functionalized MCM-41 was dried at 40 °C during 2 h.

2.3. Synthesis of DMSA-functionalized Fe_xO_y nanoparticles. Water-soluble TREG coated superparamagnetic iron oxide nanoparticles (SPIONs) were synthesized by a polyol-mediated method according to the synthesis procedure described elsewhere.²⁶⁻²⁷ DMSA-Fe_xO_y nanoparticles were obtained via a ligand-exchange reaction process described in a previous work of our laboratory²⁸ The synthesis conditions were tailored to obtain SPION nanoparticles larger than the silica pores. Briefly, a DMSA aqueous solution (30 mg mL⁻¹) was strongly mixed with a TEG-coated-SPIONs aqueous solution at room temperature. The resulting mixture was alkalinized with some drops of diluted sodium hydroxide (NaOH, 0.1 M). After NaOH addition, the suspension changed from blurred to transparent. A final step of dialysis using a 12,000-14,000-nominal molecular weight cut-off membrane (CelluSep F3, Membrane Filtration Products Inc., USA) is required in order to remove the free DMSA molecules.

2.4. Synthesis of Platinum nanoparticles. In a typical synthesis of Pt nanoparticles²⁹ 0.10 mL of H₂PtCl₆ 8 wt. % solution was added to 15 mL of distilled water in a glass vial under magnetic stirring. Hence, 0.33 mL of a 65 mM Tetrakis(hydroxymethyl) phosphonium chloride solution (THPC, 80 wt.) were subsequently added. After several minutes, 0.16 mL of a 1 M NaOH solution

was auditioned to the glass vial. The reaction mixture was kept at room temperature under moderate stirring conditions for 4 days. The product was kept in a refrigerator.

2.5. Assembly of Fe_xO_y -MCM-41 nanocomposites. The hybrid nanoparticles were fabricated by conjugation of the NH_2 functionalized mesoporous silica spheres MCM-41 with DMSA- Fe_xO_y nanoparticles by means of peptide linkers (see Figure 1). In a typical experiment, MCM-41 spheres were dissolved in water (10 mL) to a final concentration of $30 \text{ mg}\cdot\text{mL}^{-1}$. The pH of the MCM-41 solution was adjusted to pH 5.4. After that 0.05 mL of MCM-41 solution was added to 1.26 mL of water soluble Fe_xO_y nanoparticles (0.98 mg mL^{-1}) and the resulting aqueous dispersion was stirred at room temperature for 18 hours. Then the mixture was centrifuged at 12000 rpm for 10 minutes and the supernatant was removed. The particles were magnetically separated, washed twice with ethanol and redispersed in water until further use.

2.6. Assembly of Pt- Fe_xO_y -MCM-41 nanocomposites. A water dispersion of Pt nanoparticles (0.40 mL , $0.95\cdot 10^{-3} \text{ mg}\cdot\text{mL}^{-1}$) was mixed with 0.10 mL of Fe_xO_y -MCM-41NP suspension ($30 \text{ mg}\cdot\text{mL}^{-1}$). The total volume was adjusted to 0.50 mL and the resulting dispersion stirred at room temperature during 18 h. This allowed ample time for the process of particle "pumping" into the MCM-41 pores, as will be discussed later (see figure 1). Then the mixture was centrifuged at 12000 rpm for 10 minutes and the supernatant was removed. The Pt- Fe_xO_y -MCM-41Np were magnetically separated, washed twice with ethanol and redispersed in water.

2.7. Catalytic Reduction of p-Nitrophenol. Aqueous solution of 4-NP (0.01M , 0.03 mL) and NaBH_4 (0.5M , 0.2 mL) were mixed with water (2.5 mL) in a quartz cuvette with stirring. After the addition of the catalyst suspension ($0.952 \text{ mg}\cdot\text{mL}^{-1}$, 0.06 mL , $5 \mu\text{g}$ of Pt), the reaction solution was kept stirring for 30 seconds. The reaction progress, without stirring, was evaluated by taking multiple absorption spectra in the 250-500 nm spectral range at regular time intervals of 5 minutes

until the deep yellow solution became colorless. For testing the recyclability, the catalyst was magnetically recovered and re-dispersed in a solution containing fresh reactants.

2.8. Characterization techniques. Electron microscopy observations were carried out using a T20–FEI microscope with a LaB6 electron source fitted with a “SuperTwin®” objective lens allowing a point to point resolution of 2.4 Å. At least, one hundred particles were measured to evaluate the mean diameter of the particles and the standard deviation. The data were fitted with a log-normal distribution function and the logarithmic standard deviation was obtained for all the samples. High Resolution Transmission Electron Microscope (HRTEM) and Scanning Transmission Electron Microscope with high angle annular dark field detector (STEM-HAADF) were performed to determine the morphology and the crystalline structure using a FEI TECNAI F30 and FEI Titan™ Cube (80-300 kV) microscopes at an acceleration voltage of 300 kV. The samples for TEM analysis were prepared by resuspending the corresponding sample in ethanol, dropping the suspension onto a 200 mesh carbon-coated copper grid (Electron Microscopy Sciences) and letting it dry under ambient air with the aid of antipillary tweezers. The hydrodynamic size of hydrophilic suspension was evaluated in a 90 Plus dynamic light scattering (DLS) apparatus (Brookhaven). Magnetic properties were studied using a superconducting quantum interference device SQUID (model SQUID MPM-55S Quantum Design). Samples were prepared by placing 80 µL of a colloidal suspension of nanoparticles into a nonmagnetic teflon capsule sealed with a screw cap to prevent losses at reduced pressures. Magnetization curves were obtained by applying a maximum field of 20.000 Oe at 260 K. Diamagnetic contributions from the sample holder and solvent were subtracted from the curves. The iron content of the samples was determined with an accuracy of 0.17% using a Varian 50 Probe UV-visible-NIR spectrophotometer.³⁰ The UV-vis measurements were performed in the UV-visible

spectrophotometer (Varian 50 Probe) using quartz cuvettes with 1 cm optical path lengths. The Pt content was determined via inductively coupled plasma mass spectrometry (ELAN 6,000 Spectrometer PERKIN ELMER). The sample (100 μ L of final catalyst suspension) was digested by the addition of a mixture of HNO₃ /HCl (1:3 v/v, 5 mL), and the mixture was heated at 65°C for 2 h. The resultant solution was diluted with Milli Q water to a final volume of 25 mL for spectrometric analysis.

Electron tomography experiments were performed in the STEM mode using a probe corrected FEI Titan microscope, equipped with a XFEG source and operated at 80 kV acceleration voltage. The acquisition of tilt series was done automatically using the tomography Inspect-3D software, which allows the control of the specimen tilt step by step, the defocusing and the specimen drift. In the STEM mode, a projection image of the sample is obtained by scanning the sample with a focused probe in a raster pattern and for each tilt angle an image which is in fact a projection of the object within the observation direction is recorded. This image is mass-sensitive, especially if the detector collects only the electrons scattered at high angles where the diffraction Bragg contrast can be considered negligible.

The STEM-HAADF tilt series were acquired by using the HAADF detector by tilting the specimen in the angular range of $\pm 70^\circ$ using an increment of 2.5° in the equal mode, giving thus a total number of images equal to 57 images in each series. A beam convergence of 24.9 mrad half-angle could be selected. In this STEM-HAADF mode the intensity in the corresponding images is proportional to the mean atomic number of the specimen in first approximation.³¹

The recorded images of the tilt series were spatially aligned using first a rough alignment by cross correlating consecutive each two images, a fine alignment was performed using position of the small Pt particles. The alignment procedure is implemented in the IMOD software.³² For the

volume calculation, we have used iterative methods which are more accurate than the one-step ones, providing high quality reconstruction volumes even from series with a quite limited number of projections. The algebraic reconstruction techniques (ART)³³ implemented in the TomoJ plugin³⁴ working in the Image J software³⁵ were thus used to compute the reconstructed volumes. Finally, the visualization and the analysis of the final volumes were carried out using the displaying capabilities and the isosurface rendering method in the Slicer software.³⁶

3. RESULTS AND DISCUSSION

3.1. Water-stable magnetic mesoporous hybrids through peptide-like covalent assembly.

The synthetic approach of magnetic mesoporous silica is summarized in Figure 1a (see also the experimental section). MCM-41 spheres with average diameters of $71 \text{ nm} \pm 8 \text{ nm}$ were initially functionalized with 3-aminopropyltriethoxysilane (APTES) to render surface terminal NH_2 moieties and an isoelectric point at pH 6.5 (Figure 1b). Water-dispersible $7 \pm 2 \text{ nm}$ superparamagnetic iron oxide nanoparticles were synthesized by ligand exchange of triethylen glycol (TREG) by 2,3-dimercaptosuccinic acid (DMSA) after a solvothermal synthesis approach. This provided the hydrophilic magnetic nanoparticles with an excellent colloidal stability in water as has been demonstrated in previous works.²⁸ DMSA is able to form a stable covalent bond with the surface of the Fe_xO_y nanoparticles using one of the available carboxylic groups (COOH). Further stabilization of the ligand shells is achieved through intermolecular disulfide (S-S) bonds between closely spaced thiol groups. The second carboxylic group (C(=O)OH) provided the required functionality and negative charge for proper aqueous stability. The ζ -Potential of the magnetic dispersion remains negative across the entire pH range (Figure 1b). Additionally, these carboxylic groups at the surface of the Fe_xO_y nanoparticles are suitable for the later condensation

reaction with the amino (NH_2) silica groups, causing the release of a molecule of water and the creation of a peptide-like link ($-\text{C}(=\text{O})-\text{NH}-$). Uniformly coated mesoporous silica nanoparticles labelled as $\text{Fe}_x\text{O}_y\text{-MCM-41NP}$ were obtained when the reaction was carried out in the pH 4.0-5.0 range (highlighted pH range in Figure 1b).

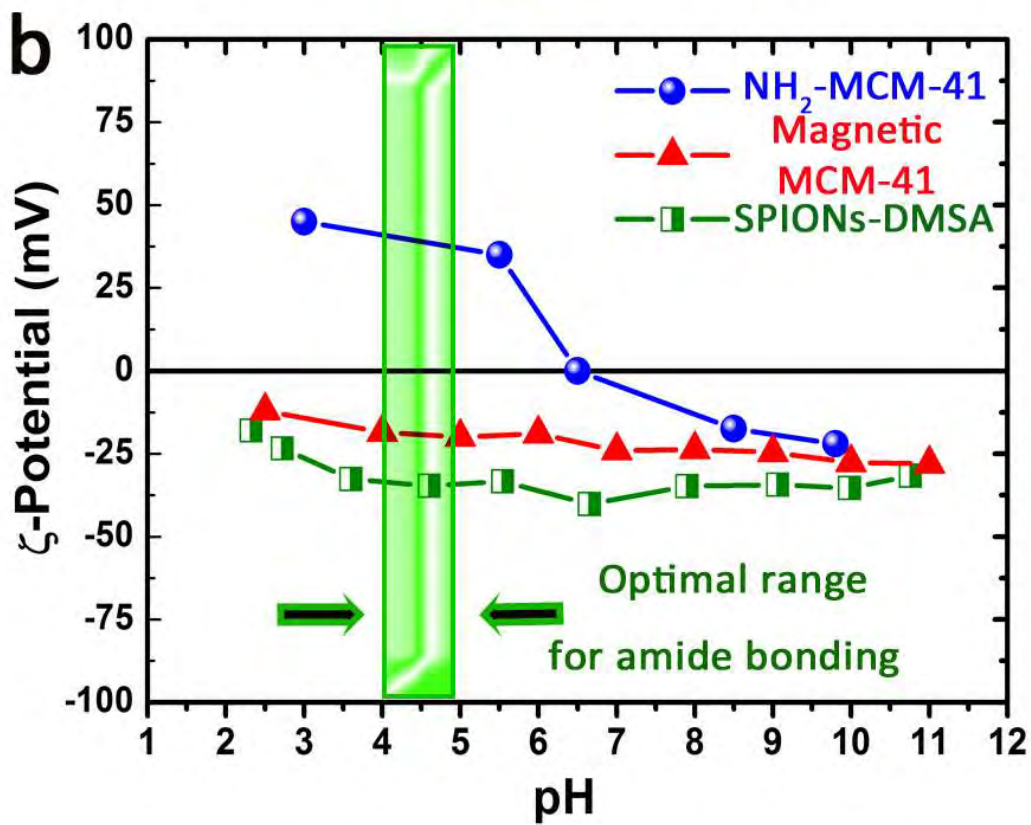


Figure 1. a) Schematic depiction of the first step: preparation of magnetic mesoporous hybrids through peptide-like covalent bounding, b) ζ -Potential as a function of pH for the mesoporous silica cores (MCM-41), freestanding Fe_xO_y NP and Fe_xO_y -MCM-41NP.

Under these conditions the DMSA-stabilized Fe_xO_y nanoparticles were covalently bonded onto the surfaces of the amino-functionalized mesoporous silica spheres. The stability of the amide covalent bonds became apparent when the hybrid particles were subjected to an environment of higher ionic strength. The magnetic nanoparticles remained attached to the surface of the mesoporous silica spheres along the whole pH range evaluated. Furthermore, the as-prepared Fe_xO_y -MCM-41NP showed a very limited aggregation in water as demonstrated by an overall hydrodynamic diameter of 175 nm (Figure S1). In contrast, when the coupling step between silica nanoparticles and Fe_xO_y NPs was carried out outside the optimum pH range (i.e. at pH values lower than 4.0 or higher than 5.0) the reaction between the magnetic nanoparticles and the mesoporous silica spheres did not yield a uniform coverage of the MCM-41 spheres (Figure S2) and the number of magnetic nanoparticles decorating the MCM-41 spheres was substantially reduced. Moreover, when the originally synthesized TREG- Fe_xO_y nanoparticles were used instead of the DMSA-stabilized ones, the assembly of the Fe_xO_y nanoparticles onto the silica spheres was unsuccessful, thereby corroborating the key role of DMSA.

Under optimum conditions, uniform 7 nm Fe_xO_y nanoparticles well assembled on the surface of the mesoporous silica spheres, with few or no aggregates of the Fe_xO_y nanoparticles present, as shown by transmission electron microscopy (TEM) observations of the hybrid nanospheres in Figure 2a. Both nanoparticle components maintained their initial sizes and properties, i.e. the well-ordered mesoporous silica structure is still clearly observed (Figure 2a) and the Fe_xO_y NPs retained a strong superparamagnetic response (vide infra). The High-Angular Annular Dark-Field

(HAADF) analysis using a scanning transmission electron microscope (STEM) (Figure 2b) corroborated the presence of Fe_xO_y nanoparticles with brighter contrast regularly attached to the surface of the mesoporous silica.

The field-dependent magnetization curve of the Fe_xO_y -MCM-41NP at 260 K shows no hysteresis (Figure S3), that is, Fe_xO_y -MCM-41NP exhibit superparamagnetic behaviour derived from the well-assembled Fe_xO_y NPs onto the mesoporous silica spheres with a magnetization value of 67 emu/g. The N_2 adsorption/desorption isotherms of the amino-functionalized MCM-41NP showed a surface area of $536 \text{ m}^2\text{g}^{-1}$ and a pore volume of $0.38 \text{ cm}^3\text{g}^{-1}$. After Fe_xO_y nanoparticles immobilization the surface area and pore volume decreased to $260 \text{ m}^2\text{g}^{-1}$ and $0.23 \text{ cm}^3\text{g}^{-1}$ respectively, still relatively large values for magnetic nanocomposites¹⁰ (Figure S4).

3.2. Pumping metal nanoparticles to design a multifunctional nanocatalyst.

Catalytic magnetic nanocomposites were fabricated by encapsulating pre-formed 1.5 nm platinum nanoparticles stabilized with tetrakis(hydroxymethyl)phosphonium chloride (THPC) within the mesoporous silica spheres (Fe_xO_y -MCM-41NP). The use of THPC as simultaneous reducing and stabilizing agent has been widely exploited for the synthesis of gold nanoparticles³⁷ but it has also been recently extended to other noble metal nanoparticles.³⁸ The assembly was carried out at room temperature in aqueous phase at a fixed pH value of 5. The process involves the electrostatic interaction between the negatively charged THPC-Pt nanoparticles (ζ -Potential = -30 mV) and the positively charged NH_3^+ mesoporous silica spheres (ζ -Potential= 27 mV) (figure 1b).

Figure 2c shows a TEM image of Pt- Fe_xO_y -MCM-41NP, where Pt nanoparticles 1.5 nm in size and 7 nm Fe_xO_y nanoparticles are assembled on 71 nm mesoporous silica spheres. The HAADF-STEM analysis shown in Figure 2d illustrates the presence of metallic Pt nanoparticles distributed

in a highly ordered manner. The high-resolution TEM (HRTEM) image shows clear crystalline magnetic Fe_xO_y nanoparticles coexisting with Pt nanocrystals (Figure S5a). A more detailed crystallographic indexation is displayed in Figure S5b. For the Fe_xO_y nanoparticles the d-spacing measured, is 2.51 Å and it can be assigned either to the (331) planes of Fe_2O_3 or of Fe_3O_4 (JCPDS file 39-1346 and 19-0629 respectively). Regarding the smaller Pt nanoparticles, the (200)-1.95Å and (220)-1.39Å planes of Pt can be clearly observed. Energy-dispersive X-ray analysis confirms the presence of O, Si, Pt and Fe which are the main components of the Pt- Fe_xO_y -MCM-41NP, indicating the high purity of the nanocomposite (Figure S6).

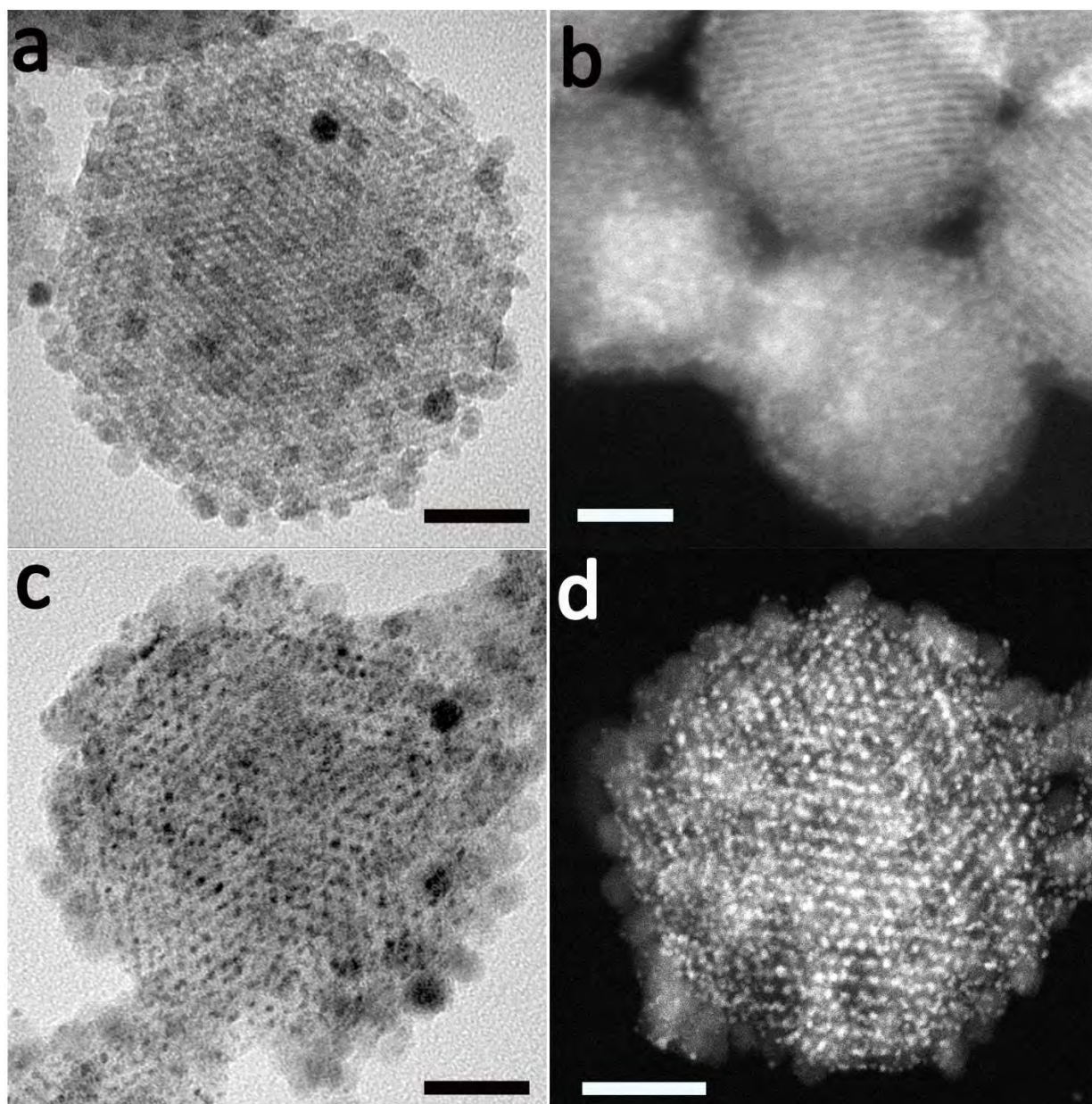


Figure 2. a) TEM image for an individual Fe_xO_y -MCM-41NP and b) STEM/HAADF image of Fe_xO_y -MCM-41NP, c) TEM image of mesoporous silica sphere assembled with 7 nm Fe_xO_y nanoparticles and 1.5 nm Pt nanoparticles, d) STEM-HAADF image of an individual Pt- Fe_xO_y -MCM-41NP. All scales bar correspond to 20 nm.

Filling the channels of ordered mesoporous materials with preformed metal nanoparticles remains as challenging task. In spite of using mesoporous supports with larger porous channels such as SBA-15 (6.8 nm in pore size),³⁹⁻⁴⁰ diffusion of the metal NPs into the nanoscale pore channels is not favored and nanoparticles clustered close to the pore openings can hinder reactant diffusion. This problem becomes more severe in the case of mesoporous supports with smaller pore size, such as MCM-41. From a practical point of view, this problem may go unnoticed, as it is challenging to differentiate whether the metal NPs are located at the pore openings, within the pore along the channels or distributed throughout the outer surface of the porous silica nanoparticles. High resolution tools now available such as 3D Tomography may provide an answer to this question, however, to the best of our knowledge, no previous studies of the distribution of pre-formed Pt NPs within MCM-41 ordered silica nanostructures have been previously reported by 3D Tomography.

To have a direct assessment of the distribution of Pt nanoparticles, a detailed three-dimensional High-Resolution HAADF electron tomography evaluation of the magnetic composite was carried out. Figure 3a illustrates two projections extracted from the tilt series at two different orientations in which one can distinguish that the small Pt nanoparticles follow the pores orientation of the grain. Yet at this stage it is still uncertain whether the Pt nanoparticles are located inside or outside the channel pores' direction. The analyses of the reconstructed volume of these grains solved this issue. In Figure 3b where transversal section through the reconstructed volume is given one can easily see that the vast majority of the small Pt nanoparticles are localized inside the channels of the grain, as observed in Figure 3c. However, a small number of Pt nanoparticles can also be identified outside the structure, more exactly on the Fe_xO_y nanoparticles. Figure 3d displays the 3-D model corresponding to the reconstructed volume of a representative Pt- Fe_xO_y -MCM-41

nanoplatfom. The granular appearance in yellow color corresponds to the Fe_xO_y nanoparticles on the outer surface. Remarkably, the presence of Pt NPs (in red color) is clearly observed in the inner pores of the mesoporous support. These findings corroborate the high selectivity for the encapsulation of the pre-formed Pt NPs within the mesoporous channels in spite of being loaded into the channels across the barrier of previously attached 7 nm magnetic nanoparticles.

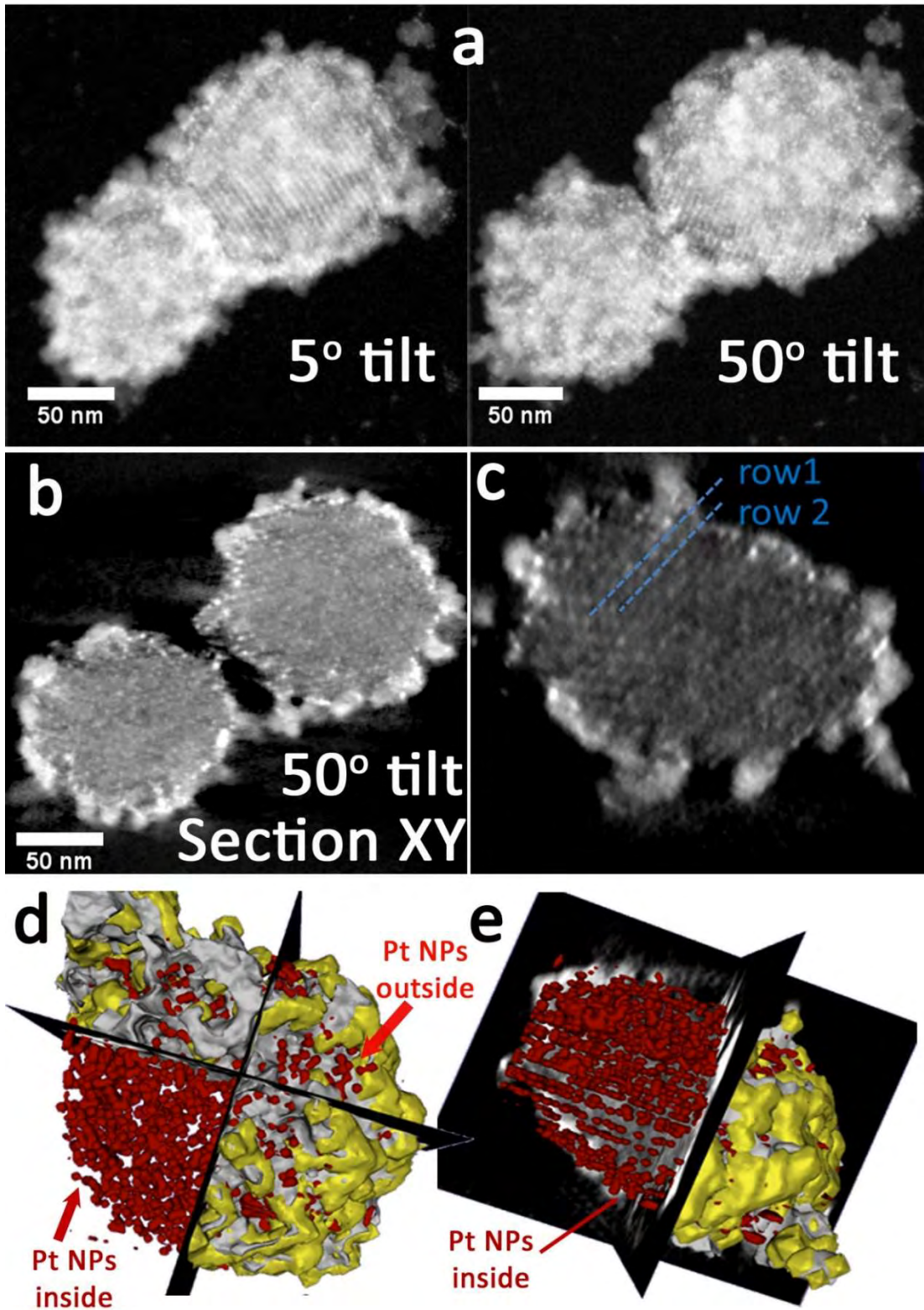


Figure 3. a) Examples of STEM-HAADF images from the tilt series used to reconstruct the volume of the studied grains, corresponding to 5 and 50 degrees tilt angles, b) Typical XY section through the reconstructed volume, showing the exact localization of both types of nanoparticles Fe_xO_y and Pt, c) Section through the reconstructed volume of one grain which was oriented in order to evidence the localization of the Pt 1.5 nm nanoparticles inside the porous structure of the composite particle, d) 3D Model of the grain in which the porous structure is represented in white, the 7 nm Fe_xO_y nanoparticles in yellow, and the small Pt nanoparticles in red, e) 3D model of one of the composite particles with the Pt nanoparticles following the pores orientation of the grain.

This high selectivity of the location of Pt nanoparticles inside the silica channels is remarkable given the pore size of the initial MCM-41 mesostructure (2.9 nm), the final size of the Pt NPs (1.5 nm, ligand distances excluded) and the fact that pore entrances are partly occluded by the grafted 7 nm, (ligand distances excluded) Fe_xO_y NPs.

In order to elucidate a mechanism capable to explain the filling of mesopores under these circumstances, several experiments were performed in the presence of different volumes of Pt NP suspension ($0.95 \times 10^{-3} \text{ mg} \cdot \text{mL}^{-1}$) containing a constant volume (100 μL) of MCM-41NP suspension ($30 \text{ mg} \cdot \text{mL}^{-1}$). In all the experiments, the mixing time was kept at 2 minutes and the pH value was fixed at 5. When 200 μL of Pt NP solution was added to 100 μL of MCM-41NP solution a considerable excess of Pt nanoparticles remaining in solution was observed even after long contact times (12 h), suggesting that the maximum loading Pt nanoparticles within the silica matrix had been reached. Figure 4d shows the transmission electron microscopy image of the obtained hybrids under the maximum load of nanoparticles: the Pt NP are encapsulated within the ordered silica structure and distributed throughout the entire MCM-41 framework, filling the pores. TEM micrographs of the particles prepared separately by adding aliquots of 10 μL , 20 μL

and 50 μL of Pt NP suspension into 100 μL of MCM-41NP suspension are showed in Figures 4a-c, respectively. Since Pt NP are covered with negatively charged ligands, their spontaneous attraction from the solution to the positively charged surface of MCM-41 leads to Pt NPs being first deposited at or near the external pore mouth (Figure 4a). At low Pt NPs concentrations levels, the Pt NPs are preferably attached to this outer section of the mesoporous support. However, as the concentration of Pt NP increases, more NPs can be accumulated at the pore entry (Figure 4b-c) and their electrostatic repulsion effectively "pumps" the particles deposited deeper down through the mesochannels. Given the dimensions of the nanoparticles and the pore channels it is unlikely that a Pt NP can skip others already attached onto the pore surfaces. Therefore, the process of pore filling must be thought of as a progressive displacement of already deposited nanoparticles deeper into the silica channels. Diffusion is also assisted by the electrostatic attraction between the Pt nanoparticles and the positively charged inner channel wall. No Pt NP diffusion within the pores occurs at pH above the isoelectric point of the MCM-41 or with a nonfunctionalized MCM-41 NP, suggesting that an electrostatic modulation might be the most important reason for creating the dynamic balance that determines the Pt NPs transport through the channel. Therefore, the penetration depth of the particles into the channels as a function of the different outside concentrations of Pt NPs can be explained as a result of the interplay between particle-wall electrostatic attraction, and the repulsive forces between neighboring Pt nanoparticles. As the concentration of Pt NPs in the surrounding solution increases, the level of pore filling keeps rising until a maximum equilibrium level is reached (Figure 4d).

As a result of cargo loading, the diffraction pattern at low-angles for the hybrids under the maximum load of Pt shows a drastic lost in reflections (110) and (200) and lower intensity in the (100) peak (Figure S7). In spite of these changes, the maintenance in the intensity of the (100)

peak pattern indicates that the mesoporous structure of the nanoparticles is still intact after the loading process. Likewise, the N₂ adsorption-desorption isotherms for these hybrids nanoparticles led to a considerable reduction in the total specific surface area, pore volume and pore size (Table S1).

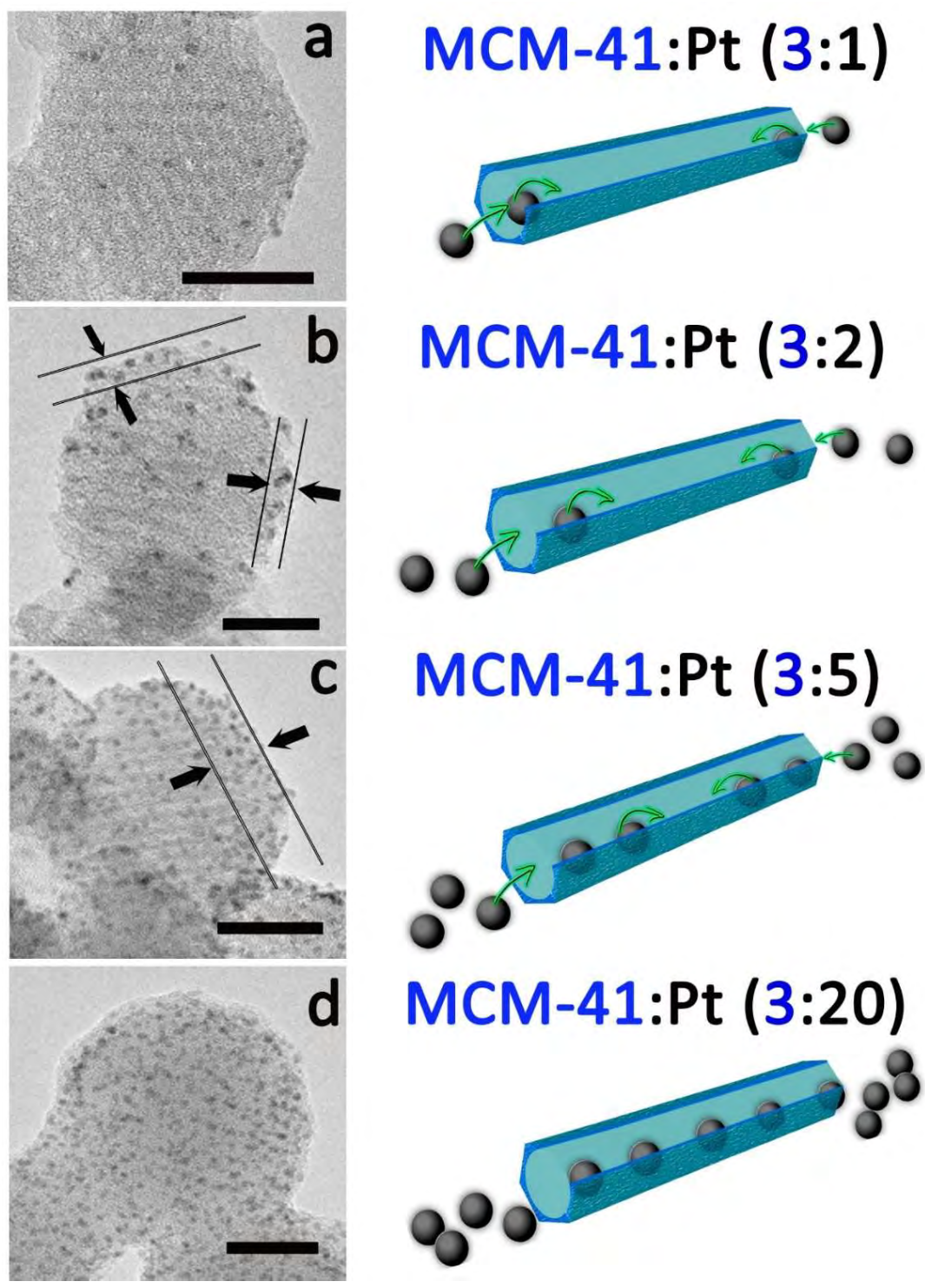


Figure 4. Scheme of the progressive filling of MCM-41 pores with preformed Pt nanoparticles and TEM images of the obtained Pt-MCM-41 NP for increasing ratios of Pt NP to MCM-41

support: a) 10 μL of Pt NP suspension (MCM-41:Pt 3:1), b) 20 μL of Pt NP suspension (MCM-41:Pt 3:2), c) 50 μL of Pt NP suspension (MCM-41:Pt 3:5) and d) 200 μL of Pt NP suspension (MCM-41:Pt 3:20) of Pt NP suspension are added to. All scales bar correspond to 20 nm.

3.3. Magnetically recoverable catalysts. To demonstrate the combined catalytic properties and magnetic manipulation capabilities of the Pt- Fe_xO_y -MCM-41NP, the selective liquid phase hydrogenation of p-nitrophenol (4-NP) by sodium borohydride was evaluated as a model reaction at ambient temperature⁴¹ (Figure 5a).

The hydrogenation of 4-NP can be monitored along the reaction time because the 4-NP absorption peak at 400 nm gradually drops in intensity⁴²⁻⁴³. Meanwhile, the formation of p-aminophenol (4-AP) can also be tracked thanks to a small shoulder at 300 nm that rises gradually. Figure 5b shows the time-dependent absorption spectra of the reaction solution with Pt- Fe_xO_y -MCM-41NP as catalyst. The absorption peak at 400 nm diminishes gradually in intensity and nearly disappears at a reaction time of 16 min, which suggests that the hydrogenation of 4-NP is complete. No hydrogenation was found to occur in the absence of the Pt NPs, which confirmed the absence of catalytic activity of the silica support or of the Fe_xO_y NPs anchored on it. Figure 5c shows the conversion profile of the catalyst, calculated as the number of moles of 4-NP hydrogenated at time t per mol of 4-NP at time $t = 0$. Since the concentration of NaBH_4 is in great excess, it can be considered as approximately constant throughout the reaction and the hydrogenation rate can be approximated by a pseudo-first-order rate kinetics with regard to the 4-NP concentration. Figure 5c also shows the plot of $\ln[C(t)/C(0)]$ against reaction time, where $C(t)$ and $C(0)$ are the concentrations of 4-NP at time t and $t = 0$, respectively. The good linear fit achieved supports the assumption of pseudo-first-order kinetics and the reaction rate constant k obtained from the slope is 0.175 min^{-1} .

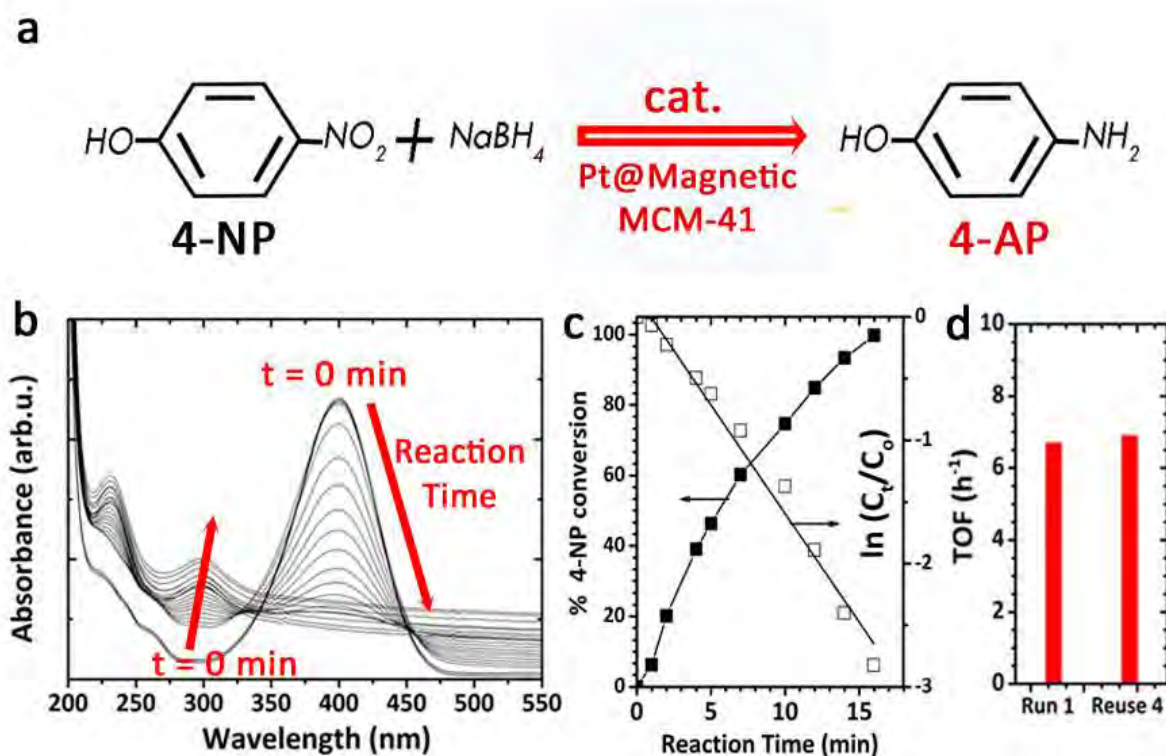


Figure 5. a) Selective hydrogenation of nitrophenol (4-NP) by sodiumborohydride (NaBH_4), b) Time-dependent absorption spectra of the reaction solution with Pt- Fe_xO_y -MCM-41NP catalyst, c) Plot of % 4-NP conversion against the reaction time and d) Comparative TOFs of the first run and after four catalytic cycles.

The k -value is comparable to the best catalysts reported in literature for 4-NP hydrogenation.⁴⁴⁻⁴⁵ This means that the catalyst Pt- Fe_xO_y -MCM-41NP is highly active for hydrogenation reaction. For industrial point of view, the possibility of catalyst recovery from the reaction products and subsequently reuse is of major importance, since it reduces the operational cost of the catalytic processes. In this case recyclability is provided by the magnetic response of the SPION shell around the composite nanoparticle. To prove the potential of Pt- Fe_xO_y -MCM-41NP as a reusable catalyst, four cycles of catalyst use with new reactants were performed, with intermediate

separation of catalyst particles from products with a magnet. The turnover frequency (TOF), defined as the moles of hydrogenated 4-NP molecules per mole of Pt atoms in the mesoporous particle per hour, was used to compare the catalytic performances in the different cycles (Figure 5d). As can be seen, the catalyst can be used repeatedly and magnetic recovery is feasible without any apparent loss in activity.

4. CONCLUSIONS

In conclusion, the method presented in this work constitutes a relatively simple and reproducible way to prepare multifunctional (magnetic-catalytic) nanosized platforms in which the three nano-components (the 70 nm silica nanoparticles as ordered mesoporous support, the 7 nm magnetite nanoparticles as the magnetic shell around them and the 1.5 nm Pt nanoparticles as the catalyst inside its pores) are assembled with a high degree of spatial accuracy. Magnetic nanoparticles were first covalently bond on the external surface of mesoporous silica spheres under mild conditions in aqueous media, and subsequently the mesoporous channels were filled by electrostatically-driven "pumping" of catalytic Pt nanoparticles. These multifunctional hybrids performed with a high catalytic activity and could be efficiently recycled using magnetic separation, with negligible catalyst loss. The robust step-by-step method presented here can be used to prepare other hybrid candidate materials for applications in other fields.

ASSOCIATED CONTENT

Additional details regarding characterization by DLS, electronic microscopy, magnetization curve and N₂ adsorption/desorption isotherms have been included as a word file of Supporting Information. This file and its content is available free of charge.

AUTHOR INFORMATION

Corresponding Author

*E-mail address: Jesus Santamaria, Jesus.Santamaria@unizar.es; Gema Martinez, gemamar@unizar.es

Notes

The authors declare no competing financial interest.

ACKNOWLEDGMENT

Financial support from MINECO (Spain) and the CIBER-BBN (financed by the Instituto de Salud Carlos III with assistance from the European Regional Development Fund) and European Research Council ERC-Advanced Grant HECTOR is gratefully acknowledged. The synthesis of materials has been performed by the Platform of Production of Biomaterials and Nanoparticles of the NANOBIOSIS ICTS, more specifically by the Nanoparticle Synthesis Unit of the CIBER in BioEngineering, Biomaterials & Nanomedicine (CIBER-BBN). The microscopy works have been conducted in the "Laboratorio de Microscopias Avanzadas" at "Instituto de Nanociencia de Aragon - Universidad de Zaragoza. V. S. and J.L.H acknowledge the support of the People Program (CIG-Marie Curie Actions, REA grant agreement no. 321642 and 294094).

REFERENCES

1. Tao, Y. F.; Lin, W. G.; Gao, L.; Yang, J.; Zhou, Y.; Yang, J. Y.; Wei, F.; Wang, Y.; Zhu, J. H. Low-Cost and Effective Phenol and Basic Dyes Trapper Derived from the Porous Silica Coated with Hydrotalcite Gel. *J. Colloid Interface Sci.* **2011**, *358* (2), 554-561.

2. Lee, C. K.; Liu, S. S.; Juang, L. C.; Wang, C. C.; Lin, K. S.; Lyu, M. D. Application of MCM-41 for Dyes Removal from Wastewater. *J. Hazard. Mater.* **2007**, *147* (3), 997-1005.
3. Vallet-Regi, M.; Ramila, A.; del Real, R. P.; Perez-Pariente, J. A new property of MCM-41: Drug Delivery System. *Chem. Mat.* **2001**, *13* (2), 308-311.
4. Laurent, S.; Forge, D.; Port, M.; Roch, A.; Robic, C.; Elst, L. V.; Muller, R. N. Magnetic Iron Oxide Nanoparticles: Synthesis, Stabilization, Vectorization, Physicochemical Characterizations, and biological Applications. *Chem. Rev.* **2008**, *108* (6), 2064-2110.
5. Na, H. B.; Hyeon, T. Nanostructured T1 MRI Contrast Agents. *J. Mater. Chem.* **2009**, *19* (35), 6267-6273.
6. Stoeva, S. I.; Huo, F. W.; Lee, J. S.; Mirkin, C. A. Three-Layer Composite Magnetic Nanoparticle Probes for DNA. *J. Am. Chem. Soc.* **2005**, *127* (44), 15362-15363.
7. Polshettiwar, V.; Luque, R.; Fihri, A.; Zhu, H. B.; Bouhrara, M.; Bassett, J. M. Magnetically Recoverable Nanocatalysts. *Chem. Rev.* **2011**, *111* (5), 3036-3075.
8. Zhang, L.; Qiao, S. Z.; Jin, Y. G.; Yang, H. G.; Budihartono, S.; Stahr, F.; Yan, Z. F.; Wang, X. L.; Hao, Z. P.; Lu, G. Q. Fabrication and Size-Selective Bioseparation of Magnetic Silica Nanospheres with Highly Ordered Periodic Mesostructure. *Adv. Funct. Mater.* **2008**, *18* (20), 3203-3212.
9. Yiu, H. H. P.; Keane, M. A.; Lethbridge, Z. A. D.; Lees, M. R.; El Haj, A. J.; Dobson, J. Synthesis of Novel Magnetic Iron Metal-Silica (Fe-SBA-15) and Magnetite-Silica (Fe₃O₄-SBA-15) Nanocomposites with a High Iron Content Using Temperature-Programed Reduction. *Nanotechnology* **2008**, *19* (25), 255606 (7pp).

10. Lee, J. E.; Lee, N.; Kim, H.; Kim, J.; Choi, S. H.; Kim, J. H.; Kim, T.; Song, I. C.; Park, S. P.; Moon, W. K.; Hyeon, T. Uniform Mesoporous Dye-Doped Silica Nanoparticles Decorated with Multiple Magnetite Nanocrystals for Simultaneous Enhanced Magnetic Resonance Imaging, Fluorescence Imaging, and Drug Delivery. *J. Am. Chem. Soc.* **2010**, *132* (2), 552-557.
11. Kim, J.; Lee, J. E.; Lee, J.; Yu, J. H.; Kim, B. C.; An, K.; Hwang, Y.; Shin, C. H.; Park, J. G.; Kim, J.; Hyeon, T. Magnetic Fluorescent Delivery Vehicle Using Uniform Mesoporous Silica Spheres Embedded with Monodisperse Magnetic and Semiconductor Nanocrystals. *J. Am. Chem. Soc.* **2006**, *128* (3), 688-689.
12. Kim, J.; Kim, H. S.; Lee, N.; Kim, T.; Kim, H.; Yu, T.; Song, I. C.; Moon, W. K.; Hyeon, T. Multifunctional Uniform Nanoparticles Composed of a Magnetite Nanocrystal Core and a Mesoporous Silica Shell for Magnetic Resonance and Fluorescence Imaging and for Drug Delivery. *Angew. Chem.-Int. Edit.* **2008**, *47* (44), 8438-8441.
13. Ruiz-Hernandez, E.; Lopez-Noriega, A.; Arcos, D.; Izquierdo-Barba, I.; Terasaki, O.; Vallet-Regi, M. Aerosol-Assisted Synthesis of Magnetic Mesoporous Silica Spheres for Drug Targeting. *Chem. Mat.* **2007**, *19* (14), 3455-3463.
14. Yi, D. K.; Lee, S. S.; Papaefthymiou, G. C.; Ying, J. Y. Nanoparticle Architectures Templated by SiO₂/Fe₂O₃ Nanocomposites. *Chem. Mat.* **2006**, *18* (3), 614-619.
15. Zhang, Y. H.; Su, Z. S.; Li, B.; Zhang, L. M.; Fan, D.; Ma, H. P. Recyclable Magnetic Mesoporous Nanocomposite with Improved Sensing Performance toward Nitrite. *ACS Appl. Mater. Interfaces* **2016**, *8* (19), 12344-12351.

16. Lin, Y. S.; Wu, S. H.; Hung, Y.; Chou, Y. H.; Chang, C.; Lin, M. L.; Tsai, C. P.; Mou, C. Y. Multifunctional Composite Nanoparticles: Magnetic, Luminescent, and Mesoporous. *Chem. Mat.* **2006**, *18* (22), 5170-5172.
17. Alam, S.; Anand, C.; Logudurai, R.; Balasubramanian, V. V.; Ariga, K.; Bose, A. C.; Mori, T.; Srinivasu, P.; Vinu, A. Comparative Study on the Magnetic Properties of Iron Oxide Nanoparticles Loaded on Mesoporous Silica and Carbon Materials with Different Structure. *Microporous Mesoporous Mat.* **2009**, *121* (1-3), 178-184.
18. Wang, X. Q.; Chen, M.; Li, L.; Jin, D. F.; Jin, H. X.; Ge, H. L. Magnetic Properties of SBA-15 Mesoporous Nanocomposites with CoFe₂O₄ Nanoparticles. *Mater. Lett.* **2010**, *64* (6), 708-710.
19. Perez, J. M.; Josephson, L.; O'Loughlin, T.; Hogemann, D.; Weissleder, R. Magnetic Relaxation Switches Capable of Sensing Molecular Interactions. *Nat. Biotechnol.* **2002**, *20* (8), 816-820.
20. Berret, J. F.; Schonbeck, N.; Gazeau, F.; El Kharrat, D.; Sandre, O.; Vacher, A.; Airiau, M. Controlled Clustering of Superparamagnetic Nanoparticles Using Block Copolymers: Design of New Contrast Agents for Magnetic Resonance Imaging. *J. Am. Chem. Soc.* **2006**, *128* (5), 1755-1761.
21. Josephson, L.; Perez, J. M.; Weissleder, R. Magnetic Nanosensors for the Detection of Oligonucleotide Sequences. *Angew. Chem.-Int. Edit.* **2001**, *40* (17), 3204-3306.
22. Kim, J.; Park, S.; Lee, J. E.; Jin, S. M.; Lee, J. H.; Lee, I. S.; Yang, I.; Kim, J. S.; Kim, S. K.; Cho, M. H.; Hyeon, T. Designed Fabrication of Multifunctional Magnetic Gold Nanoshells

and Their Application to Magnetic Resonance Imaging and Photothermal Therapy. *Angew. Chem.-Int. Edit.* **2006**, *45* (46), 7754-7758.

23. Kim, J.; Lee, J. E.; Lee, J.; Jang, Y.; Kim, S. W.; An, K.; Yu, H. H.; Hyeon, T. Generalized Fabrication of Multifunctional Nanoparticle Assemblies on Silica Spheres. *Angew. Chem.-Int. Edit.* **2006**, *45* (29), 4789-4793.

24. Zeng, W.; Qian, X. F.; Zhang, Y. B.; Yin, J.; Zhu, Z. K. Organic Modified Mesoporous MCM-41 Through Solvothermal Process as Drug Delivery System. *Mater. Res. Bull.* **2005**, *40* (5), 766-772.

25. Yague, C.; Arruebo, M.; Santamaria, J. NIR-Enhanced Drug Release from Porous Au/SiO₂ Nanoparticles. *Chem. Commun.* **2010**, *46* (40), 7513-7515.

26. Cai, W.; Wan, J. Q. Facile Synthesis of Superparamagnetic Magnetite Nanoparticles in Liquid polyols. *J. Colloid Interface Sci.* **2007**, *305* (2), 366-370.

27. Miguel-Sancho, N.; Bomati-Miguel, O.; Roca, A. G.; Martinez, G.; Arruebo, M.; Santamaria, J. Synthesis of Magnetic Nanocrystals by Thermal Decomposition in Glycol Media: Effect of Process Variables and Mechanistic Study. *Ind. Eng. Chem. Res.* **2012**, *51* (25), 8348-8357.

28. Miguel-Sancho, N.; Bomati-Miguel, O.; Colom, G.; Salvador, J. P.; Marco, M. P.; Santamaria, J. Development of Stable, Water-Dispersible, and Biofunctionalizable Superparamagnetic Iron Oxide Nanoparticles. *Chem. Mat.* **2011**, *23* (11), 2795-2802.

29. Hueso, J. L.; Sebastian, V.; Mayoral, A.; Uson, L.; Arruebo, M.; Santamaria, J. Beyond Gold: Rediscovering Tetrakis-(hydroxymethyl)-phosphonium Chloride (THPC) as an Effective

Agent for the Synthesis of Ultra-Small Noble Metal Nanoparticles and Pt-Containing Nanoalloys. *RSC Adv.* **2013**, 3 (26), 10427-10433.

30. Adams, P. E. Determining Iron Content In Foods By Spectrophotometry. *J. Chem. Educ.* **1995**, 72 (7), 649-651.

31. *Scanning Transmission Electron Microscopy*. Springer. Berlin ed.; 2001.

32. Mastronarde, D. N. Dual-axis Tomography: An Approach with Alignment Methods that Preserve Resolution. *J. Struct. Biol.* **1997**, 120 (3), 343-352.

33. Richard Gordon, R. B., Gabor T. Herman Algebraic Reconstruction Techniques (ART) for three-Dimensional Electron Microscopy and X-ray Photography. *J. Theor. Biol.* **1970**, 29 (3), 471-476, IN1-IN2, 477-481.

34. Mihalek, I.; Res, I.; Lichtarge, O. Background Frequencies for Residue Variability Estimates: BLOSUM Revisited. *BMC Bioinformatics* **2007**, 8, 488 (8pp).

35. <http://u759.curie.e-psud.fr/software-su759.html>.

36. <http://www.slicer3d.org>.

37. Duff, D. G.; Baiker, A.; Edwards, P. P. A New Hydrosol of Gold Clusters .1. Formation and Particle-Size Variation. *Langmuir* **1993**, 9 (9), 2301-2309.

38. Uson, L.; Sebastian, V.; Mayoral, A.; Hueso, J. L.; Eguizabal, A.; Arruebo, M.; Santamaria, J. Spontaneous Formation of Au-Pt alloyed Nanoparticles Using Pure Nano-Counterparts as Starters: a Ligand and Size Dependent Process. *Nanoscale* **2015**, 7 (22), 10152-10161.

39. Lee, I.; Zhang, Q.; Ge, J. P.; Yin, Y. D.; Zaera, F. Encapsulation of Supported Pt Nanoparticles with Mesoporous Silica for Increased Catalyst Stability. *Nano Res.* **2011**, *4* (1), 115-123.
40. Song, H.; Rioux, R. M.; Hoefelmeyer, J. D.; Komor, R.; Niesz, K.; Grass, M.; Yang, P. D.; Somorjai, G. A. Hydrothermal Growth of Mesoporous SBA-15 Silica in the presence of PVP-Stabilized Pt Nanoparticles: Synthesis, Characterization, and Catalytic Properties. *J. Am. Chem. Soc.* **2006**, *128* (9), 3027-3037.
41. Pradhan, N.; Pal, A.; Pal, T. Silver Nanoparticle Catalyzed Reduction of Aromatic Nitro Compounds. *Colloid Surf. A-Physicochem. Eng. Asp.* **2002**, *196* (2-3), 247-257.
42. Hayakawa, K.; Yoshimura, T.; Esumi, K. Preparation of Gold-Dendrimer Nanocomposites by Laser Irradiation and Their Catalytic Reduction of 4-Nitrophenol. *Langmuir* **2003**, *19* (13), 5517-5521.
43. Praharaj, S.; Nath, S.; Ghosh, S. K.; Kundu, S.; Pal, T. Immobilization and Recovery of Au Nanoparticles from Anion Exchange Resin: Resin-Bound Nanoparticle Matrix as a Catalyst for the Reduction of 4-Nitrophenol. *Langmuir* **2004**, *20* (23), 9889-9892.
44. Lee, J.; Park, J. C.; Song, H. A nanoreactor Framework of a Au@SiO₂ yolk/shell Structure for Catalytic Reduction of p-Nitrophenol. *Adv. Mater.* **2008**, *20* (8), 1523-1528.
45. Jin, Z.; Xiao, M. D.; Bao, Z. H.; Wang, P.; Wang, J. F. A General Approach to Mesoporous Metal Oxide Microspheres Loaded with Noble Metal Nanoparticles. *Angew. Chem.-Int. Edit.* **2012**, *51* (26), 6406-6410.

Table of Contents Graphic

